東京大学　大学院　新領域創成科学研究科　物質系専攻　修士論文

$SrTiO_3$ field effect transistor with $SrTiO_{3-\delta}$ source and drain electrodes

$SrTiO_{3-\delta}$をソース・ドレイン電極に用いた$SrTiO_3$電界効果トランジスタ

指導教員　：　ミック・リップマー　助教授

56120

佐藤　泰輔

2007 年 1 月 30 日

$SrTiO_3$ field effect transistor with $SrTiO_{3-\delta}$ source and drain electrodes

Contents

Capter1. General Introduction

1-1 Introduction 3
1-2 Transition metal oxides 4
1-3 Physical properties of $SrTiO_3$ 7
1-4 Purpose of this study 8
References 9

Capter2. Fabrication and characterization techniques of oxide thin films

2-1 Pulsed laser deposition (PLD) 11
2-2 Deposition control system 13
2-3 Reflection high-energy electron diffraction (RHEED) 15
2-4 Atomic force microscopy (AFM) 16
2-5 Optical measurement 16
2-6 Electrical measurement 17

Chapter3. Lithography and Etching

3-1 Introduction 19
3-2 Photoresist 20
3-3 Photomasks and Patten transfer 21
3-4 Argon ion milling 23
References 23

Chapter4. Fabrication and characterization of oxygen-deficient $SrTiO_{3-\delta}$ layers

4-1 Introduction 25
4-2 fabrication and characterization $SrTiO_{3-\delta}$ 26
4-2 Conclusions 34
References 35

平成十八年度修士論文

$SrTiO_{3-\delta}$をソース・ドレイン電極に用いた$SrTiO_3$電界効果トランジスタ

佐藤　泰輔

Chapter5. Fabrication and insulating properties of amorphous and epitaxial $CaHfO_3$ films

5-1 Introduction 36
5-2 Fabrication and insulating properties of $CaHfO_3$ films 37
5-2 Growth of epitaxial $CaHfO_3$ films 41
5-2 $SrTiO_3$ substrates 43
5-3 Conclusion 46
References 47

Chapter6. Fabrication and electronic properties of $SrTiO_3$-based field-effect transistors with amorphous insulator layers

6-1 Introduction 48
6-2 New fabrication process of $SrTiO_3$ FETs 49
6-3 Characterization of $SrTiO_3$ FETs with an amorphous $CaHfO_3$ gate insulator 53
6-4 Fabrication and Characterization of $SrTiO_3$ FETs with an epitaxial $CaHfO_3$ gate insulator 62
6-5 Fabrication and Characterization of $SrTiO_3$ FETs with an amorphous $CaHfO_3$ gate insulator for 4-point measurements of channel resistivity 66
References 73

Chapter7. Conclusion 75

Achievement Lists 77

Acknowkedgements 78

Chapter 1

General Introduction

1-1 Introduction

The quest for ever higher operating speeds and higher levels of integration continue to drive extensive research projects aimed at developing innovative electronic devices. Further scaling of device structures based on well-established semiconductor materials like silicon is getting harder, particularly in the areas of large-scale integrated circuits and high-density data storage. Due to this, many research groups have turned their attention to various new materials, such as transition-metal oxides. Oxides are among the best candidates for developing new innovative electronic devices that may surpass traditional silicon in performance. In oxides, it is possible to manipulate spin ordering, spin transport, charge ordering, and even orbital ordering, prompting the design of new types of electronic devices based on, for example, ferroelectrics[1], high-T_c superconductors[2], colossal magnetoresistance(CMR)[3], and colossal electroresistance(CER)[4].

Due to these interesting properties, I have focused in this work on the electronic properties of transition-metal oxides, with a particular focus on perovskite-type materials. Transition-metal oxides exhibit various potentially useful electronic properties, but the utilization of these materials in high-quality devices is still very limited in practical applications. One of the main reasons for that is the difficulty of controlling the electrical properties of oxide heterointerfaces. Understanding the formation of electronic states at oxide heterointerfaces is indispensable for realizing high-performance devices, because most device applications rely on heterostructures.

1-2 Transition metal oxides

First, it is worthwhile to sketch the background as to why the perovskite-related transition metal oxides are useful building blocks for novel electronics.

Most compounds with the general formula ABO_3 have the perovskite structure or at least a distorted perovskite structure. The atomic arrangement in this structure was first found in the mineral 'perovskite' $CaTiO_3$. The unit cell of ABO_3 is cubic, with the A ions at the corners of the cube and B ions at the body center position. The three oxygen ions are at the centers of the unit cell faces (Figure 1). In perovskite-type oxides, the A-site cation is coordinated with twelve oxygen ions, and the B cation with six. Thus, the ionic radius of the A cation is normally found to be somewhat larger than that of the B cation. Therefore, the largest number of perovskite-type compounds are described by the general formula $A^{2+}B^{4+}O_3$, where the A^{2+} cations are alkaline-earth ions, cadmium, lead and so on, while the B^{4+} cations are transition metals and some rare-earth ions, which are, in general, smaller than the cations of the A site. A diagrammatic presentation of the crystal structure with respect to the ionic radii of the A and B cations for the $A^{2+}B^{4+}O_3$ and $A^{3+}B^{3+}O_3$ type compounds are shown in Figures 2 (a) and (b), respectively[5].

The BO_6 octahedron in a perovskite oxide ABO_3 forms a three-dimensional network. If the system is metallic, electric conduction is three-dimensional along the BO_6 network. From the point of view of transport properties, an important advantage of the perovskite structure therefore is the stability of the BO_6 network under substitutions of the A-site cations. Perovskite ABO_3 oxides with transition-metal cations at the B site provide us with an ideal setting to study the effects of electron correlations. The A-site cation is completely ionized in most cases without contributing to the band formation. The electronic properties are almost entirely determined by electrons left in the oxygen $2p$ bands and the transition metal d bands. With this advantage, we can employ three strategies for a systematic control of the electronic states in ABO_3 compounds[6]:

(1) Band filling control. The number of conduction electrons per unit formula is controlled by a chemical substitution of an A-site ion with another ion of different valence. Band filling can also be controlled by charge transfer, photocarrier injection, and field effect.

(2) Bandwidth control. B-O-B bond angle can be changed by changing the ionic radius of the A-site ion or subjecting thin oxide films to epitaxial strain. In case of chemical substitutions, the bond-angle buckling is governed by the tolerance factor f, which is defined for the perovskite ABO_3 structure as

$$f = \frac{R_A + R_O}{\sqrt{2}(R_B + R_O)}$$

where R_A, R_O and R_B are the ionic radii of the A-site ion, the oxygen ion, and the B-site ion, respectively. When the value of f is close to 1, the system is cubic; while for $f < 1$, the lattice structure changes to rhombohedral or orthorhombic types. In the orthorhombic perovskite

structure, it is known that the B-O-B bond angle decreases continuously with decreasing f almost irrespective of the set of A and B [7]. The buckling of the B-O-B bond angle reduces the conduction band width, since the effective d-electron transfer interaction between the neighboring B sites is governed by the transfer process via the O $2p$ states. Thus, the ratio of Coulomb interaction to bandwidth can be systematically controlled by substitutions or strain, since bond angle changes do not affect the electron interaction energy at the B sites.

(3) Dimensional control. By changing the crystal structure from a simple perovskite to a layered perovskite, such as A_2BO_4 or by studying oxide nanostructures and superlattices, it is possible to follow how the electronic states change as the electrons are confined to lower than three dimensions.

These principles form the basis for systematic research of perovskite transition metal oxides. In this thesis I mostly rely on the first strategy, i.e. a systematic control of carrier density in a $SrTiO_3$ single crystal by field effect.

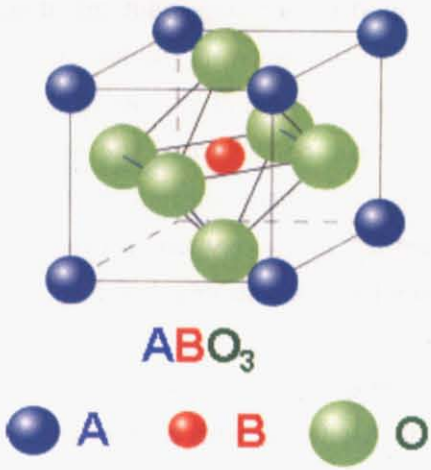

Figure1. ABO_3 crystal structure.

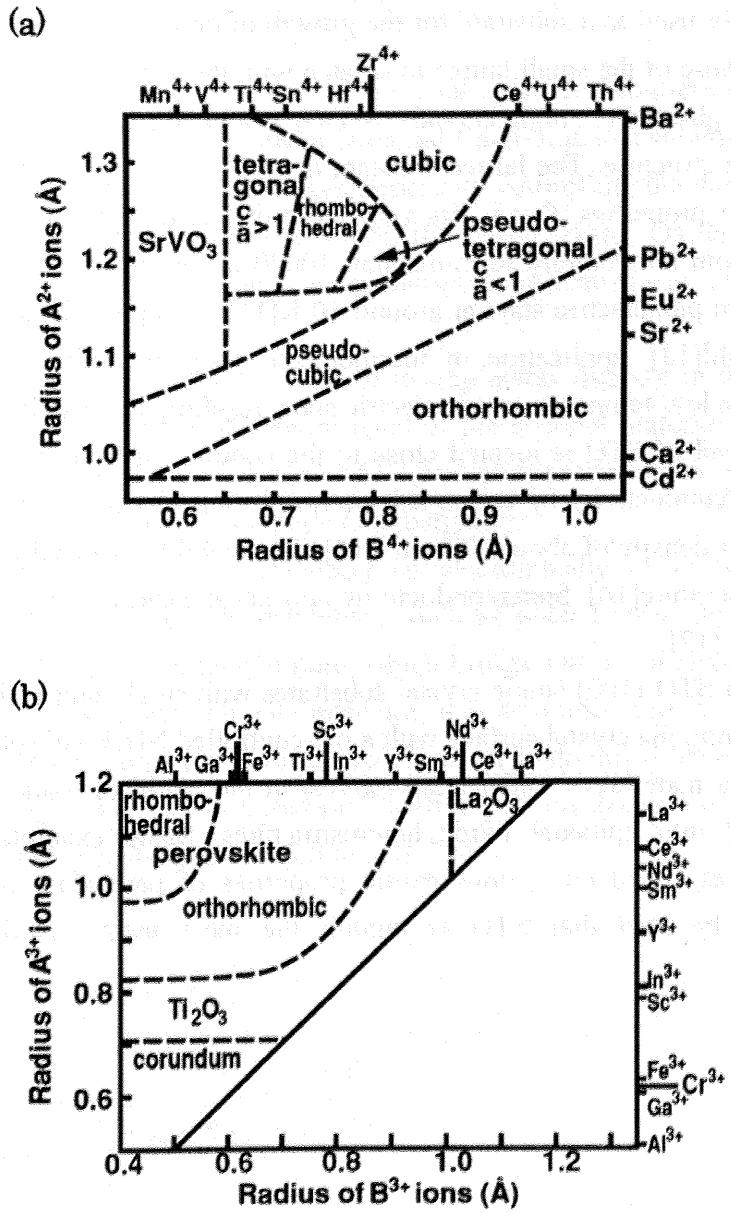

Figure2. Classification of perovskite type compounds (a) $A^{+2}B^{+4}O_3$ and (b) $A^{+3}B^{+3}O_3$ [Ref. 5].

1-3 Physical properties of $SrTiO_3$

$SrTiO_3$ is widely used as a substrate for the growth of perovskite-type transition-metal oxide films partly because of the small lattice mismatch with these materials and also because of the availability of high-quality single crystals. $SrTiO_3$ is a band insulator ($E_{gap}\approx3.2$ eV[8]) with a cubic perovskite structure. The lattice constant is 3.905 Å[9]. It has long been studied for its unique dielectric properties, that is, its very large dielectric constant, which increases from about 300 at room temperature to more than 10000 at low temperature[10] as the material enters a quantum paraelectric state at around 10 K[11]. Isotopic substitution[12], application of electrical field[13], application of thermoelectric[14], or application of stress[15], can easily disturb the low-temperature paraelectric state, resulting in ferroelectricity.

The Fermi level of STO is located close to the conduction band bottom and it is easy to induce metallic conductivity by cation substitution or introduction of oxygen deficiency at a fairly low carrier density of about 10^{18} cm^{-3}[16]. The mobility of metallic STO increases with decreasing temperature[16]. Superconductivity appears at a carrier concentration range of 10^{19} cm^{-3} – 10^{21} cm^{-3} [17].

Atomically flat STO (100) single crystal substrates with single unit cell height steps can be obtained by etching the crystal surface with a pH-controlled NH_4F-HF solution[18].

$SrTiO_3$ has is a material of widespread interest in the world of oxide electronics and it is often integrated into epitaxial oxide heterostructures. Many examples of prototypes of electronic devices based on various exotic properties of perovskite oxides already exist. Hence, it can be said that STO is among the most used materials in these oxide heterostructures.

1-4 purpose of this study

The purpose of this study is the development of a new process for fabricating $SrTiO_3$ field-effect transistors (FETs).

In order to probe the electronic structure of epitaxial oxide heterointerfaces, $SrTiO_3$ (100) single crystal FETs with either amorphous or epitaxial $CaHfO_3$ gate insulator layers have been used [19, 20]. These devices are useful for systematically controlling the density of carriers in a thin channel layer at the topmost surface of a $SrTiO_3$ single crystal. Oxide FETs can thus be used to probe the electronic structure and carrier transport mechanisms as a function of carrier density.

The field-effect mobility of a FET is sensitive to trap states that are in the vicinity of the channel interface and also close to the Fermi level of the channel material. We can thus use the analysis of the temperature dependence of FET transport properties to obtain information on the presence of interface states in an oxide heterostructure.

The biggest technical difficulty is obtaining an electronically clean heterointerface by conventional oxide thin film growth techniques, such as pulsed laser deposition. Epitaxial layers need to be grown at a high temperature, which brings additional challenges because in addition to the channel layer and the gate insulator, it is also necessary to integrate metallic source and gate electrodes into a transistor device. In order to do this, I have developed a new process for fabricating $SrTiO_3$ FETs based on $CaHfO_3$ gate insulators and source and drain electrodes composed of metallic oxygen-deficient $SrTiO_{3-\delta}$.

References

1. C. H. Ahn, S. Gariglio, P. Paruch, T. Tybell,L. Antognazza, and J. –M. Triscone, Science. **284**, 1152 (1999).
2. J. G Bednorz and K. A. Müller, Z. Phys. **B 64**, 189 (1986).
3. Y. Tomioka, A. Asamitu, Y. Moritomo and Y. Tokura, J. Phys. Soc. Jpn , **64**, 3626 (1995).
4 A. Asamitu, Y. Tomioka, H.Kawahara and Y. Tokura, Nature, **388**, 50 (1997).
5. F. S. Galasso, Structure, Properties and Preparation of Perovskite-Type Compounds (Pergamon, Oxford, 1969), p3.
6. A. Fujimori, J. Phys. Chem. Solids. **53**, 1595 (1992).
7. M. Marezio, J. P. Remeika and P. D. Demier, The crystal chemistry of the rare earth orthoferrites Acta Crystallogr. **B 26**, 2008 (1970).
8. M.Cardona, Phys.Rev. **A 651**, 140, (1965).
9. K.H.Hellwege, A.M.Hellwege Science and Technology New Series, Group III, **Vol.16a**, 59-64 (Springer, Berlin, 1981).
10. T. Sakudo and H. Unoki, Phys. Rev. Lett. **26**, 851 (1971).
11. K. A. Müller and H. Burkard, Phys. Rev. **B 19**, 3593 (1979).
12. M.Itoh, R.Wang, Y.Inaguma, T.Yamaguchi, Y-J.Shan and T.Nakamura, Phys. Rev. Lett. **82**, 3540 (1999).
13. J.Hamberger, P.Lunkenheimer, R.Viana, R. Böhmer and A. Loidl, Phys. Rev. **B 52**, 13159 (1995).
14. H. Ohta, S. Kim, Y. Mune, T. Mizoguchi, K. Nomura, S. Ohta, T. Nomura, Y. Ikuhara, M. Hirano, H. Hosono and K. Koumoto, Nat. Mater. **6**, 129 (2007).
15. H. Uwe and T. Sakudo, Phys. Rev. **B 13**, 271 (1976).
16. O.N.Tufte and P.W.Chapman, Phys. Rev. **155**, 796 (1967).
17. J.F.Schooley, H.P.R.Frederikse, W.R.Hosler and E.R.Pfeiffer Phys. Rev. **159**, 301 (1967).
18. M.Kawasaki, K.Takahashi, T.Maeda, R.Tsuchiya, M.Shinohara, O.Ishiyama, T.Yonezawa,

M.Yoshimoto and H.Koinuma, Science **266**, 1540 (1994).

19. K.Shibuya, T.Ohnishi, M.Lippmaa, M.Kawasaki and H.Koinuma, Appl. Phys. Lett. **85**, 425 (2004).
20. K.Shibuya, T.Ohnishi, T.Uozumi, T.Sato, M.Lippmaa, M.Kawasaki and H.Koinuma, Appl. Phys. Lett. **88**, 212116 (2006).

Chapter 2

Fabrication and characterization techniques of oxide thin films

2-1 Pulsed laser deposition (PLD)

Pulsed laser deposition (PLD) is a versatile thin film deposition technique, where material is evaporated from a solid target with a laser pulse and transferred, through a gas phase, to the growth front of a film. A unique feature of PLD is that the energy source (pulsed laser) is outside of the deposition chamber and the main advantage of PLD is the nearly stoichiometric transfer of material from a solid target with the desired stoichiometry to the growing film. Solid oxide targets are commonly made by standard powder ceramic techniques, where the desired composition can be obtained by simply mixing precursors in suitable weight ratios.

Thin film growth is done at background gas pressures ranging from ultra-high vacuum (UHV) up to pressures on the order of a few Torr. The film deposition chamber can reach base pressures of $\approx 10^{-10}$ Torr, and a load-lock chamber is used for changing samples and targets to keep the main chamber clean. A vacuum pump can be attached directly to the chamber with a gate valve. A photograph of the compact PLD chamber used in this work is shown in Figure 2.1. The cylindrical chamber had a diameter of 200mm and a height of 300mm.

In the present work, a KrF excimer laser (Lambda-Physik Compex 102) was used for ablating ceramic targets. The laser discharge voltage was kept at 27 kV in order to avoid changes of the laser beam divergence. Light from the laser was directed into the vacuum chamber with a single mirror at a 30-degree angle to the target surface. Low-energy edges of the beam were removed with an aperture and the final pulse energy was adjusted with variable optical attenuator. The vacuum chamber used a synthetic quartz window for the laser entry port. The focusing lens position was changeable in order to adjust the power density at the target surface. The distance between the focus lens and the ablation targets was approximately 290 mm. The ablation laser usually illuminated an area of about 0.5 mm^2 on the target surface. The oxide target surface would be eroded quickly if the laser pulses were continuously fired at the same spot. To avoid such erosion, the targets were continuously rotated. A schematic view of the PLD chamber is shown in Figure 2.2.

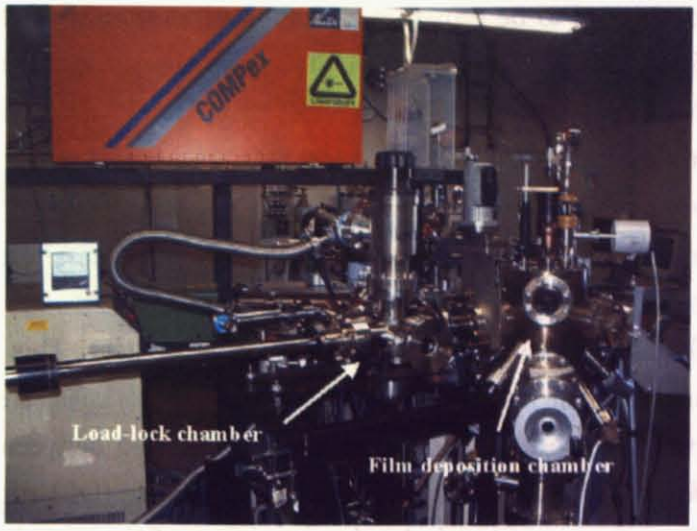

Figure 2.1 Photograph of the film deposition chamber.

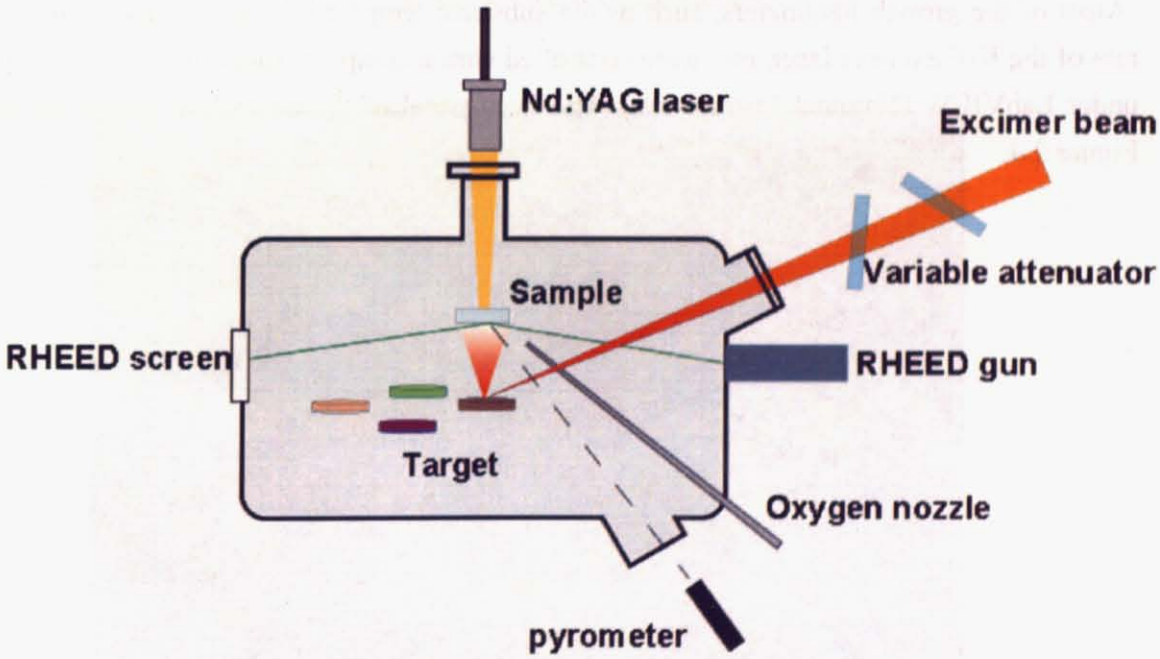

Figure 2.2 Schematic drawing of the deposition system.

2-2 Deposition control system

Many oxide materials need to be grown at elevated temperature to obtain a suitable crystal structure, phase, domain structure, lattice orientation or simply to improve crystallinity. A continuous wave Nd:YAG laser (λ=1064nm,NEC SL117) was used for substrate heating, allowing the growth temperature to reach ≈1400 °C. The temperature of the substrate was monitored with an optical pyrometer.

The substrates were clamped on a stainless steel sample holder. The sample stack on the sample holder consisted of a sapphire sheet that served as a mechanical support. A 0.05mm thick oxidized nickel sheet was mounted on the sapphire sheet. This sheet served as an absorber for the infrared light from the Nd:YAG heating laser. Substrates were mounted on top of this nickel sheet. Several thin metal foils were inserted between the heat-absorbing nickel sheet and the substrate crystal. Typically three foils a Au (0.01 mm) / Ni (0.005mm) / Au (0.01mm) configuration were used. A schematic view of the sample holder is shown in Figure 2.3.

The distance between the substrate and oxide target was usually about 50mm, but easily tunable. The background oxygen gas was introduced into the chamber with a manual molecular leak valve and the gas flow was directed at the sample surface with a nozzle.

Most of the growth parameters, such as the substrate temperature, pulse number and pulse rate of the KrF excimer laser, etc. were controlled with a computer running a control program under LabVIEW (National Instruments). The front panel of the control system is shown in Figure 2.4.

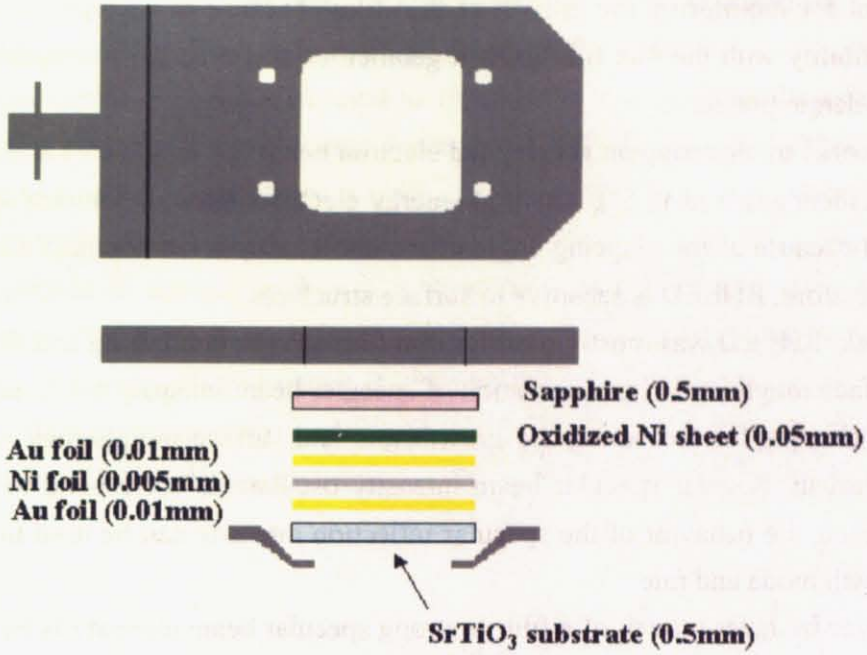

Figure 2.3 Schematic view of the sample holder.

Figure 2.4 Image of the LabVIEW control panel.

2-3 Reflection high-energy electron diffraction (RHEED)

Reflection high-energy electron diffraction (RHEED) has become an important surface analysis tool for monitoring the growth of thin films because of its high surface sensitivity and compatibility with the thin film growth geometries and even the presence of background gases at moderate pressures.

RHEED works by directing an accelerated electron beam (10 to 30 keV) at a crystal surface at a low incident angle (3 to 5°). The high-energy electrons strongly interact with the sample surface and because of the glancing angle of incidence, only a few topmost atomic layers are probed. Therefore, RHEED is sensitive to surface structures.

In this work, RHEED was mostly used for thin film growth monitoring and the investigation of film surface roughness. The observation of specular beam intensity oscillations is the most common technique for measuring the growth rate and surface morphology changes during thin film growth. Regular specular beam intensity oscillations correspond to layer-by-layer growth. Hence, the behavior of the specular reflection intensity can be used to determine the crystal growth mode and rate.

During layer-by-layer growth of a film, a strong specular beam intensity is be obtained from an atomically flat crystal surface. At the beginning of a deposition, the intensity drops quickly due to the scattering from precursor islands that form on the sample surface during the growth of the first monolayer. When the density of precursors that contribute to scattering reaches a maximum, at approximately half a monolayer coverage, the specular reflection intensity is at its minimum. After that, the remaining pits in the surface are gradually filled, and the electron beam intensity gradually recovers as a smooth surface morphology is restored. Finally, when a complete monolayer has been deposited, the intensity recovers to the original level. The deposition rate can be determined from the period of this oscillation.

2-4 Atomic force microscopy (AFM)

Scanning probe microscopes such as atomic force microscopes (AFM) are used to visualize the surface morphology of samples. Height information is obtained in an AFM by raster-scanning a probe needle over a rectangular area of the surface.

Several measurement modes can be used to obtain information about the surface topology and composition. In this study, dynamic force mode (DFM) was used. When a sample is brought close to a vibrating cantilever, a weak interaction force exists between the surface of the sample and the cantilever, resulting in an amplitude change and a phase shift. The vibration amplitude is detected with a split photodiode sensor. By adjusting the tip height during a scan so that there is no loss of vibration amplitude, a topographic image can be obtained. The resolution of the system is determined by the diameter of the tip and it is routinely possible to achieve nm order spatial resolution. In this study, Nanopics 1000, SPI3800N with SPA400 (Seiko Instruments), and SPM-9600 (SHIMADZU) microscopes were used.

2-5 Optical measurement

The focus of this work was the use of oxygen-deficient metallic $SrTiO_{3-\delta}$ layers for constructing source and drain electrodes for transistor devices. Ion milling combined with photoresist patterning was used to selectively create oxygen deficient regions in $SrTiO_3$ substrates. Optical absorption measurements were used to characterize the density of carriers generated by the milling procedure. The transmittance of milled $SrTiO_3$ was measured with a JASCO V570 UV-VIS-NIR spectrometer. The samples used in optical measurements were milled with Ar ion plasma. The milling results will be shown in Chapter4.

2-6 Electrical measurement

In most measurements, the transport characteristics of complete field-effect transistors (FETs) were studied in this work. In some cases, insulating properties such as breakdown field and leak current density were also measured.

Insulating properties were investigated mainly by current-voltage (IV) measurements at room temperature. Transport measurements of the FETs were performed in a manual probing station (Figure 2.5) (OYAMA CO,.LTD) and a liquid He flow-type cryostat (Model Helitran LT-3-110, Advanced Research Systems, Inc.). Several types of FETs were measured. In most cases, the channel current was measured in a two-point setup, only contacting the source and drain electrodes. Several FETs were also fabricated with two additional electrodes either crossing the channel region or attaching to the side of the channel area. These additional electrodes were used for 4-point measurements of channel resistivity. The measurement geometry and a photograph of a device are shown in Figure 2.6. In this measurement system, a number of current sources, current meters, and voltmeters were used, including a 6485 picoammeter, 6487 picoammeter/voltage source, 6517A electrometer (KEITHLEY) and a 7651 DC source (YOKOGAWA). The 6517A electrometer (KEITHLEY) has very high input impedance, over 200 TΩ. A device under measurement is shown in Figure 2.6. In Other measurements, such as leak characterization, a 4200 semiconductor characterization system (KEITHLEY) was used together with a manual probing station at room temperature. In addition, a Lake Shore 330 Auto tuning temperature controller was used in low-temperature measurements of the FETs..

Hall measurements were performed in a physical property system (Quantum Design, PPMS) up to a magnetic field of 5 T using the van der Pauw technique.

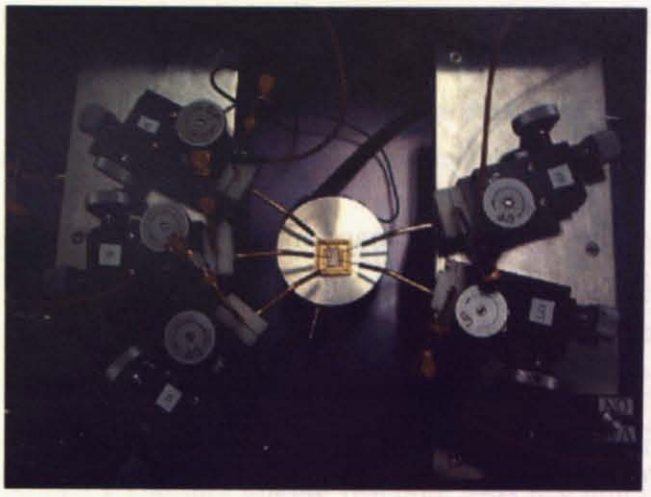

Figure 2.5 Photograph of a manual probing station.

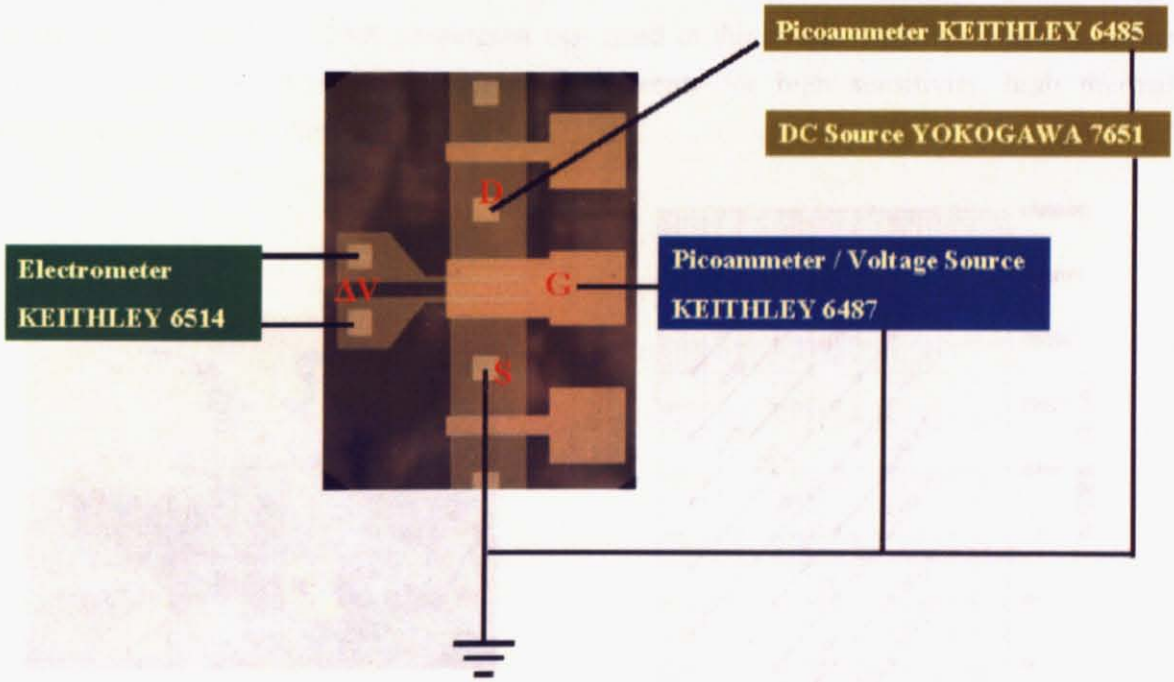

Figure 2.6 Schematic drawing of the measurement system for FETs with two potential probes inside the channel region.

Chapter 3

Lithography and Etching

3-1 Introduction

Photolithography is the process of transferring patterns of geometric shapes on a photomask to a thin layer of light-sensitive photoresist covering the surface of a sample. The patterns on a mask define the various regions in a device, such as the milling regions, the contact windows, and the bonding-pad areas.

All lithographic processes must be performed in a clean environment. All devices described in this work were prepared in JIS CLASS 5 cleanroom. The particle density was monitored with a particle counter. Figure 3.1 (a) shows the particle-size distribution curves for various classes of clean room. Figure3.1 (b) shows a photograph of the cleanroom in Lippmaa laboratory. In this section I describe the equipment used for photolithography and the basic photolithography techniques.

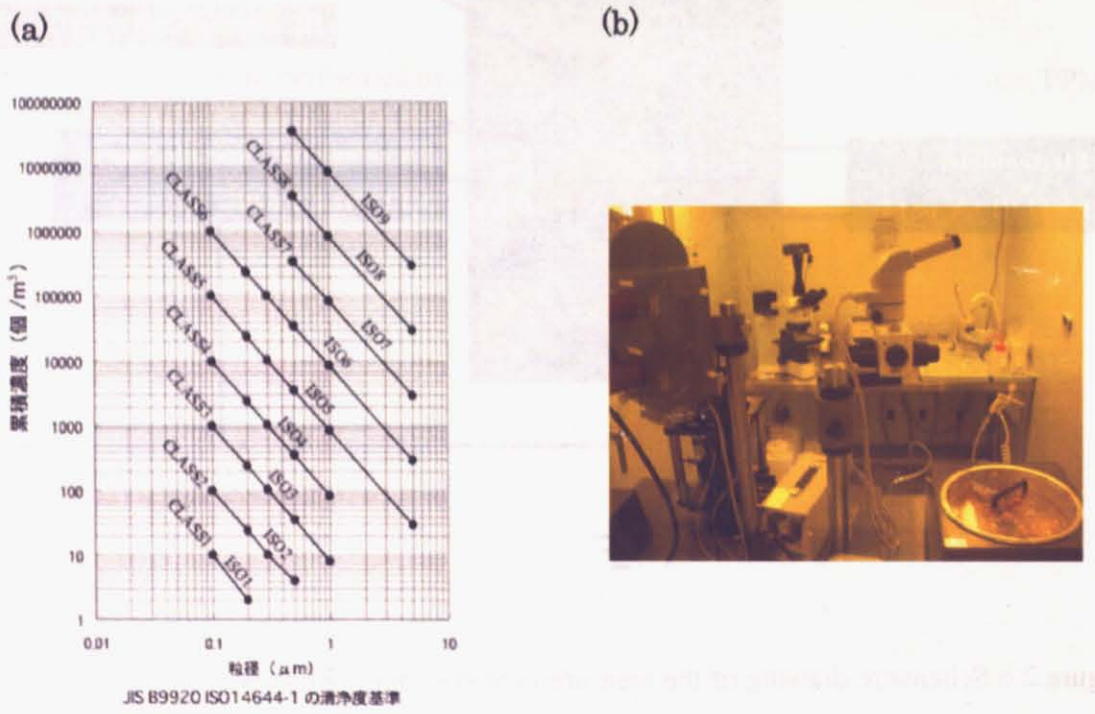

Figure 3.1 (a) Particle-size distribution for JIS standard cleanrooms. (b) Photograph of the cleanroom.

3-2 Photoresist

The photoresist is a light-sensitive compound. Resists are classified as positive and negative, depending on how they respond to light. For a positive resist, the exposed regions become more soluble and thus more easily removed in the development process. The result is that the patterns formed in a positive resist are identical to those on the mask. For a negative resist, the exposed regions become less soluble, and the pattern formed on the sample surface is the inverse of the mask pattern.

Positive photoresists consist of three components: a photosensitive compound, a base resin, and an organic solvent. Prior to exposure, the photosensitive compound is insoluble in the developer solution. After development, the exposed areas are removed.

Negative photoresists consist of a polymer combined with a photosensitive compound. During exposure, the photosensitive compound absorbs the optical energy and converts it into chemical energy to initiate a polymer linking reaction. This reaction causes cross linking of the polymer molecules. The cross-linked polymer has a higher molecular weight and becomes insoluble in the developer solution. After development, the unexposed areas are removed. One major drawback of a negative photoresist is that in the development process, the whole resist mass swells by absorbing developer solvent. This swelling action limits the resolution of negative photoresists.

A Rohm and Haas S9912NX photoresist was used in this work. This is a positive G-line resist optimized to satisfy fine process requirements for high sensitivity, high thermal resistance and high resolution.

3-3 Photomasks and Patten transfer

Figures 3.2 (a), (b), (c), and (d) show the patterns used in the FET process photomasks. At the first step in this study, FETs were fabricated using the mask patterns shown in Figures 3.2 (a) and (b). These masks use the same device size as was used in previous work but a different fabrication process [1].

The sample processing was done in a cleanroom, which was illuminated with yellow light, since photoresists are not sensitive to wavelengths greater than 0.5 μm. The sample was held on a vacuum spindle, and a small amount of photoresist was applied to the center of the sample. The sample was then rapidly accelerated up to a constant rotation speed. In this work, the spin coating was done in two steps. After spinning at 2000 rpm for 5 seconds, the sample rotation was accelerated to 5000 rpm, which was maintained for 30 seconds to obtain a uniform film coating with a thickness of about 1 μm. The thickness of the photoresist layer is correlated with its viscosity. After spinning, the sample was subjected to a soft bake (typically at 100 °C for 13 minutes) to remove the solvent from the photoresist film and to increase resist adhesion to the sample. The sample was aligned with respect to the photomask in an optical mask aligner system, and the resist was exposed to UV light using an ultra-high pressure mercury lamp. Finally, the unexposed areas of the photoresist were removed in a lift-off process. In the lift-off process, a Rohm and Haas MF CD-26 developer was used. After all these photolithography steps, the photomask pattern was transferred to the sample surface.

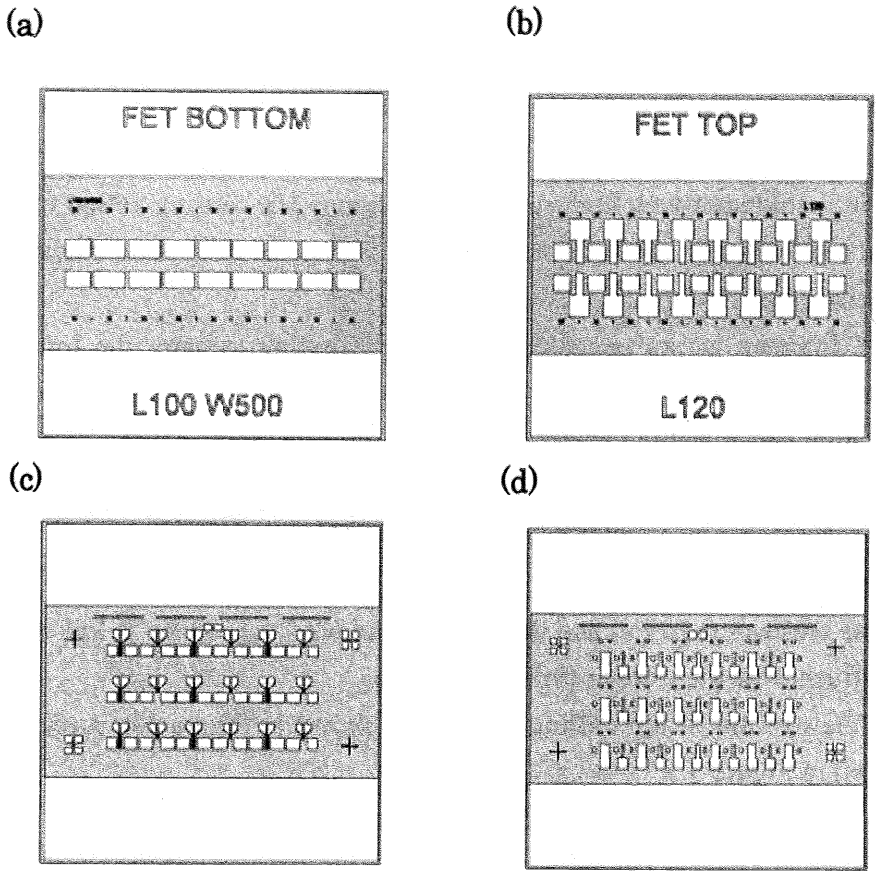

Figure 3.2 Schematic drawing of photomasks.

3-4 Argon ion milling

Figure 3.3 shows the ECR-type Ar ion milling system used for fabricating the electrode regions of the FETs. A 2.45 GHz microwave source was used to ionize the gas. The plasma generator also used a magnet to force the electrons into circular orbits. The electron cyclotron resonance conditions were satisfied in this system at a magnetic field of 875 Gauss, significantly increasing the ionization efficiency. In this way, a highly ionized plasma could be generated in a comparatively high degree of vacuum. The milling action of the plasma is achieved by accelerating the ions at an acceleration voltage of 500V, and placing a sample on a cooled stage in the path of the high-energy Ar ions.

Since a hot filament is not used in this type of milling system, the ion source is not damaged even if reactive gases are used for sample processing. Therefore, it is possible to perform good high-speed etching using reactant gas for selectivity. Moreover, since etching is done by ions that move essentially along a straight path, high resolution patterns can be etched into the sample surface with high aspect ratios.

In this system, Ar gas was used and the gas flow was set at 10 sccm. Since etching can be done at low gas pressure (~20 Pa) and the background pressure can be as low as 10^{-5} Pa, there is also little influence on the sample from residual gas.

A schematic view of the Ar ion milling machine is shown in Figure 3.4. A photograph of the system is shown in Figure 3.5.

Reference

1. K.Shibuya, T.Ohnishi, M.Lippmaa, M.Kawasaki and H.Koinuma, Appl. Phys. Lett. **85**, 425 (2004).

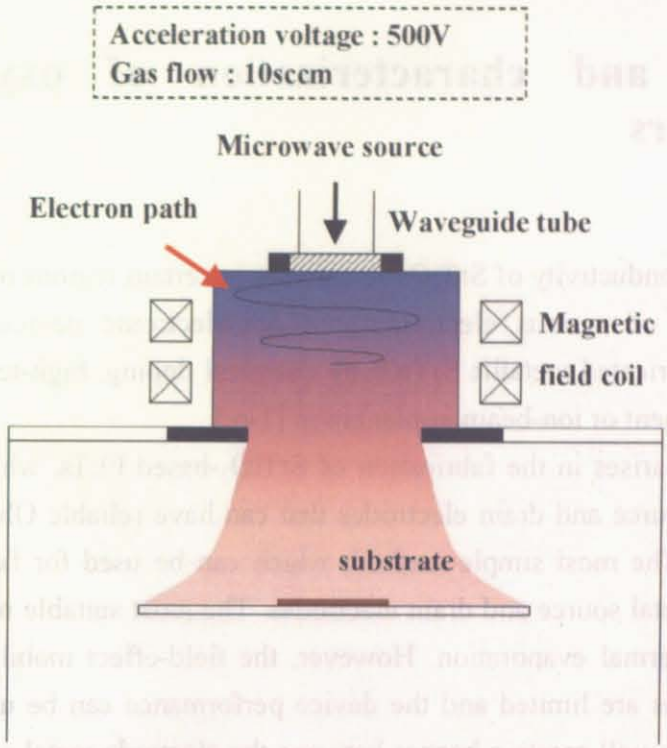

Figure 3.3 Schematic drawing of the Ar ion milling system.

Figure 3.4 Photograph of the Ar ion milling machine.

Chapter 4

Fabrication and characterization of oxygen-deficient $SrTiO_{3-\delta}$ layers

4-1 Introduction

Manipulating the conductivity of $SrTiO_3$ selectively in certain regions of a substrate is useful for the fabrication of various electronic and optoelectronic device structures. Various researchers have fabricated metallic $SrTiO_3$ by chemical doping, high-temperature reduction, noble-ion bombardment or ion-beam implantation [1-6].

A similar problem arises in the fabrication of $SrTiO_3$-based FETs, where it is necessary to fabricate metallic source and drain electrodes that can have reliable Ohmic contact with the transistor channel. The most simple method, which can be used for fabricating amorphous devices, is to use metal source and drain electrodes. The most suitable material appears to be Al, deposited by thermal evaporation. However, the field-effect mobility of FETs that use aluminium electrodes are limited and the device performance can be unpredictable because even slight oxidation will create a barrier between the electrode metal and the oxide channel [7,8]. To address these issues, I developed a technique for fabricating thermally stable oxygen-deficient and defect-rich $SrTiO_3$ layers for the purpose of building device electrodes. Selective modification of the conductivity of the $SrTiO_3$ substrate surface in the electrode regions was done by Ar ion milling the substrate through a photoresist mask. Oxygen-deficient $SrTiO_{3-\delta}$ was efficiently formed by Ar ion milling at an acceleration voltage of 500 V at a 10 sccm gas flow rate. This is an efficient way of introducing oxygen vacancies into a thin surface layer of $SrTiO_3$. These vacancies function as donors, inducing metallic conductivity in the milled regions.

In this section, I consider the fabrication and characterization of the oxygen-deficient $SrTiO_{3-\delta}$ layer.

4-2 fabrication and characterization $SrTiO_{3-\delta}$

It is known that the surface of a single-crystal $SrTiO_3$ substrate can be transformed into a high-quality, nearly transparent conducting nanolayer using Ar ion milling. A single crystal (100)-oriented $SrTiO_3$ substrate was etched in NH_4F-HF prior to use and the presence of a step-and-terrace surface structure was verified by atomic force microscopy (AFM). An AFM image of single crystal $SrTiO_3$ substrate (Shinkosya) is shown in Figure 4.1 (a). The insulating (100) single crystal $SrTiO_3$ substrate surface was converted into a high-quality conducting nanolayer using Ar ion milling. An AFM image of the milled surface of a single-crystal $SrTiO_3$ substrate is shown in Figure 4.1 (b). The milling destroyed the original step-and-terrace surface but left behind a defect-rich layer that contained enough oxygen vacancies to induce metallic conductivity. It is known generally that oxygen vacancies in $SrTiO_3$ function as donors. The depth of milling $SrTiO_3$ samples for several milling times are shown in Figure 4.2. The etching rate was estimated to be about 5.8 nm min^{-1}.

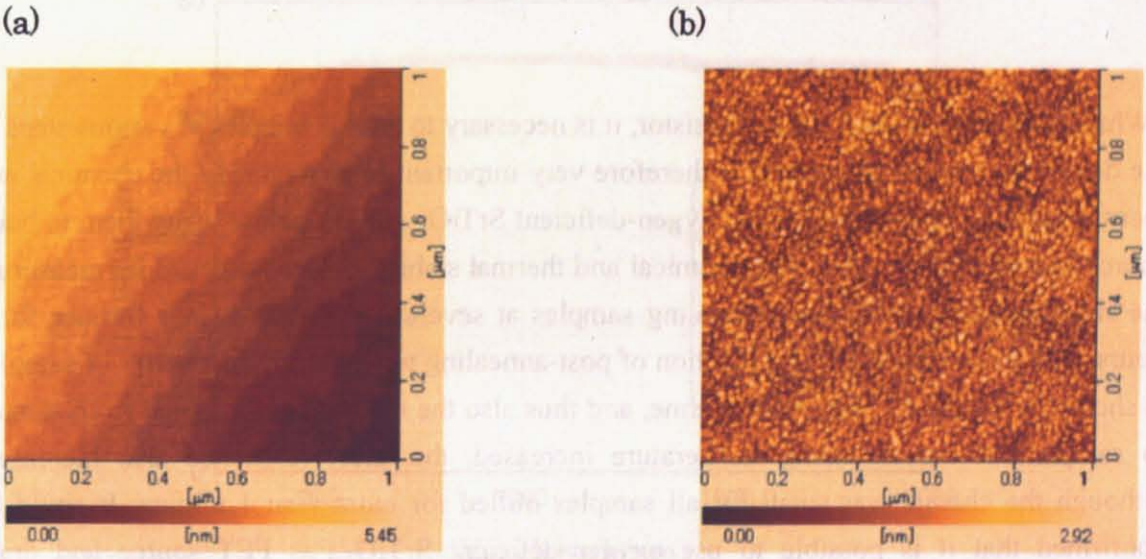

Figure4.1 AFM images of (a) commercial and (b) Ar ion milled $SrTiO_3$ (100) substrates. The image sizes are 1×1 μm^2.

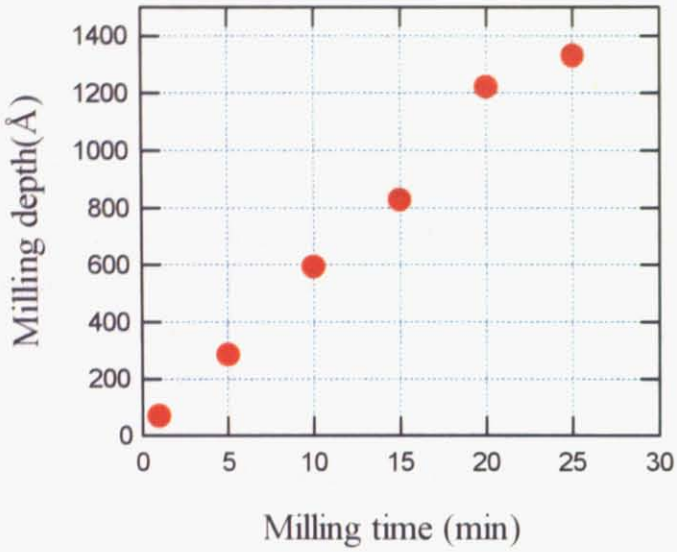

Figure4.2 Milling depth of $SrTiO_3$ as a function of milling time.

When fabricating a field effect transistor, it is necessary to anneal samples at various steps in the device fabrication process. It is therefore very important to characterize the chemical and thermal stability of the ion-milled oxygen-deficient $SrTiO_{3-\delta}$ layers before using them to build source and drain electrodes. The chemical and thermal stabilities were checked by measuring the sheet resistance after post-annealing samples at several temperatures in a furnace for 2 hours. The sheet resistance as a function of post-annealing temperature for a series of samples is shown in Figure 4.3. The milling time, and thus also the milling depth, varied from sample to sample. As the annealing temperature increased, the sheet resistance also increased, although the change was small for all samples milled for more than 1 minute. It could be confirmed that it is possible to use oxygen-deficient $SrTiO_{3-\delta}$ as FET source and drain electrodes, even in a process that requires moderate heat treatment after electrode fabrication. For comparison, the sheet resistance of a $SrTiO_3$ transistor channel, where conductivity is induced by field effect, is on the order of 10^5 Ω at room temperature.

The optical transmittance of the milled $SrTiO_3$ samples was measured with a spectrophotometer. The transmittances for several milling times are shown in Figure 4.4. There were almost no differences between the milled $SrTiO_3$ samples, even for long milling times because the oxygen-deficient $SrTiO_{3-\delta}$ layer is very thin. It is thus possible to fabricate field-effect devices that are transparent in the visible range.

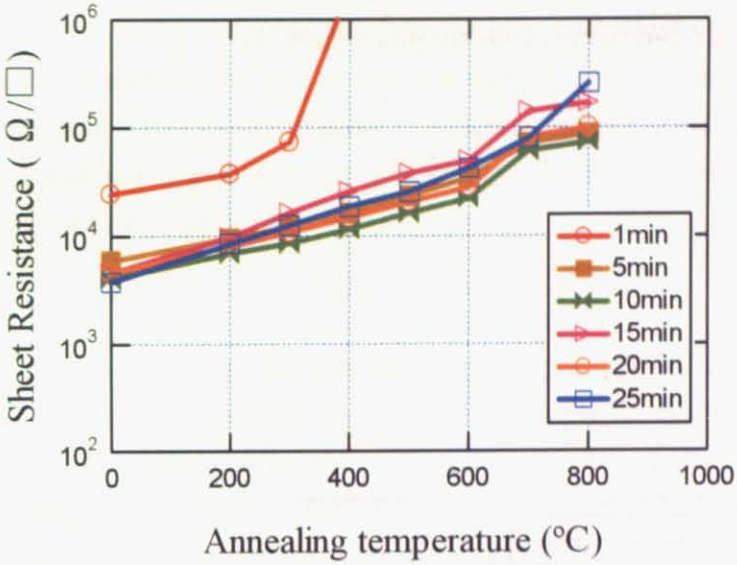

Figure4.3 The sheet resistances as a function of post-annealing at various milling times.

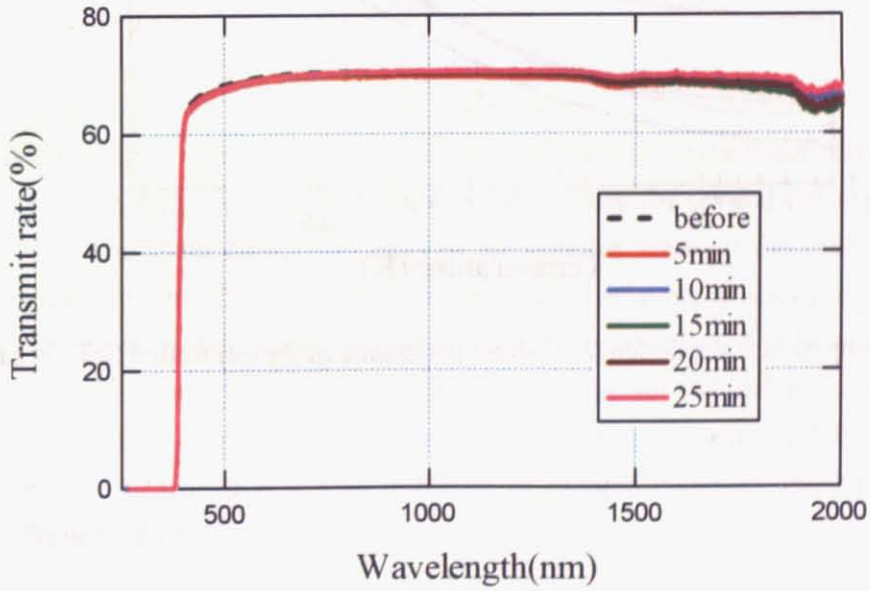

Figure4.4 Optical transmittance of ion-milled $SrTiO_3$ for several milling times.

The temperature dependence of the sheet resistance of Ar-milled $SrTiO_3$ samples is shown in Figure 4.5. Metallic behaviour was seen in all samples. The behaviour is similar to oxygen-deficient and Nb-doped $SrTiO_3$ single crystals [1].

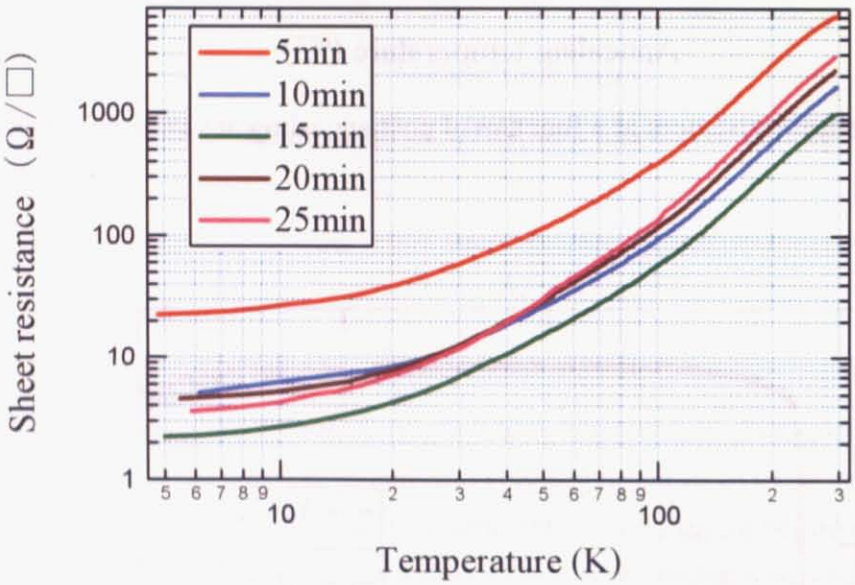

Figure4.5 The temperature dependence of sheet resistance of Ar ion milled $SrTiO_3$ samples.

The van der Pauw method is a commonly used technique to measure the Hall effect in thin film samples. Hall measurements were performed in a physical property measurement system at magnetic fields of up to 5 T. The van der Pauw technique is illustrated in Figure 4.6(a). To determine the mobility and density of carriers in a sample, four electrodes are formed at the corners of a rectangualr substrate and current is injected into electrodes (1) and (3) (I_{13}). The voltage between contacts (2) and (4) (V_{24}) is measured. From these two values, a resistance ($\Delta R_{ac,bd}$) can be found using Ohm's law:

$$\Delta R_{13,24} = \frac{V_{24}}{I_{13}}$$

The result of the measurement at 80 K is shown in Figure 4.6(b). The polarity of the Hall voltage indicates the type of dominant carriers in the sample; if the voltage is positive, the material is p-type, if the voltage is negative, the material is n-type. According to this rule, it could be confirmed that the majority carriers in the oxygen-deficient $SrTiO_{3-\delta}$ layer were electrons, since the slope of the resistance plot was negative.

The sheet carrier density can be shown to be

$$n_{\square} = \frac{B}{e \cdot \Delta R_{13,24}}$$

This can then be rearranged to give the majority carrier mobility in terms of the previously measured sheet resistance and sheet carrier density

$$\mu = \frac{1}{B} \cdot \frac{\Delta R_{13,24}}{\rho_{\square}}$$

where e is elementary charge, B is the magnetic field and $\rho_{\square}$ is the sheet resistance.

The temperature dependence of the sheet carrier density for several milling times are shown in Figure 4.7. The sheet carrier densities of all samples were on the order of 10^{14} and thus high enough for the use of the oxygen-deficient $SrTiO_{3-\delta}$ layers as source and drain electrodes in FETs. The effective sheet carrier density in an FET was expected to be of order of 10^{12}.

The temperature dependence of the Hall mobility for several milling times are shown in Figure 4.8 (a), which shows similar behavior as oxygen-deficient and Nb-doped $SrTiO_3$ [1]. The temperature dependence of Hall mobility of oxygen-deficient and Nb-doped $SrTiO_3$ is shown in Figure 4.8 (b) for comparison.

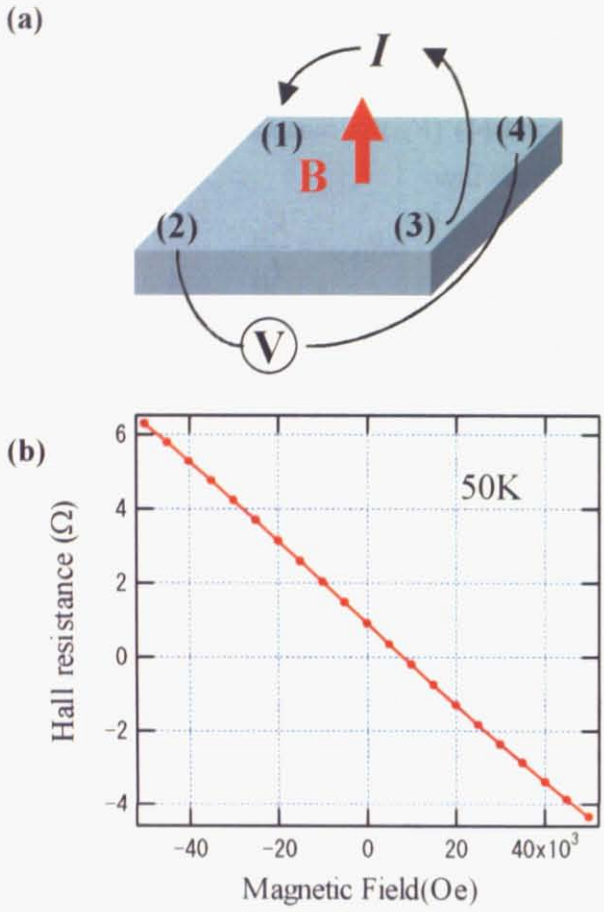

Figure 4.6 (a) Schematic image of the van der Pauw technique. (b)The result of a Hall measurement at 80 K.

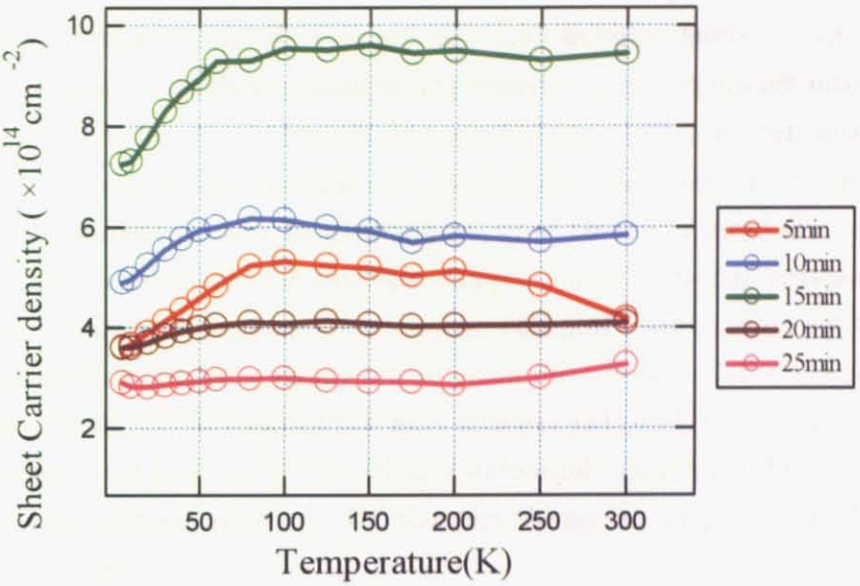

Figure4.7 Temperature dependence of sheet carrier density for several milling times.

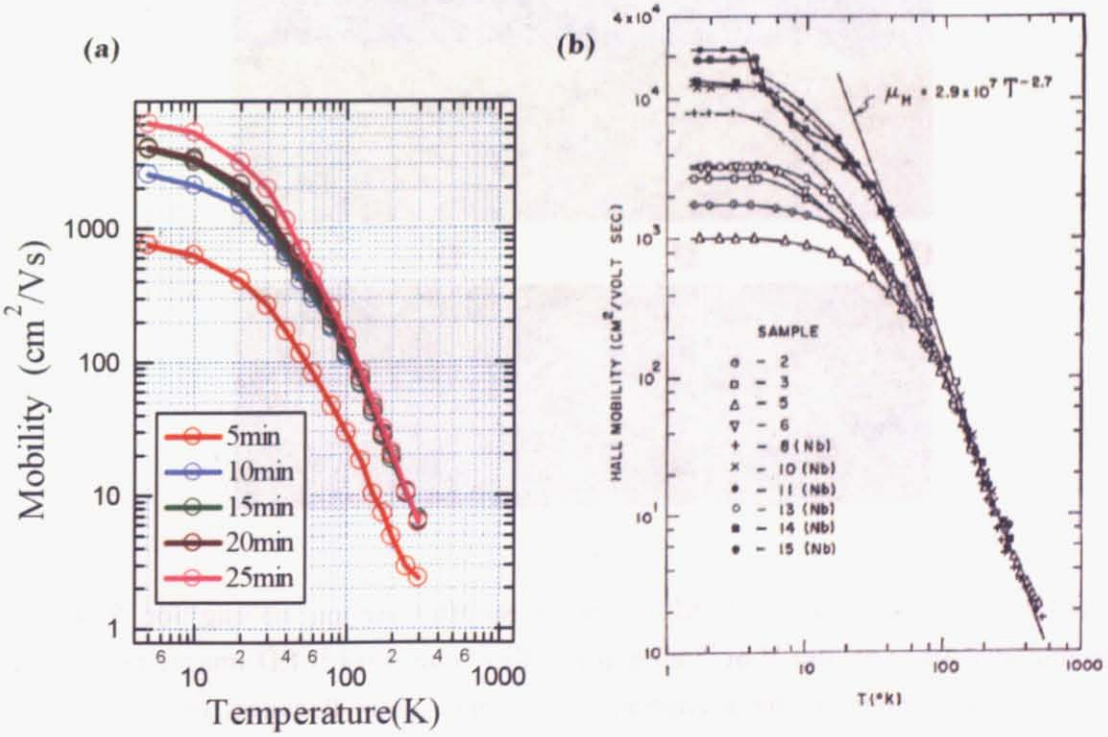

Figure4.8 (a) Temperature dependence of Hall mobility for several milling times, (b) the temperature dependence of Hall mobility of oxygen-deficient and Nb-doped $SrTiO_3$ [Ref. 1].

The thickness of the oxygen-deficient $SrTiO_{3-\delta}$ layer was not directly measured in this work. However, there are some reported thickness estimates. In one case, the layer thickness was calculated from the ion penetration length [5]. In another published report, the thickness was measured from electron diffraction (ED) images of sample cross-sections [6]. The ED images are shown in Figure 4.9 (a), (b), (c) and (d). The thickness of the oxygen-deficient $SrTiO_{3-\delta}$ layer was in both cases estimated to be on the order of several nanometers. Based on these reports, the carrier densities of the oxygen-deficient $SrTiO_{3-\delta}$ layers prepared in this work would be of the order of 10^{21}. It is also interesting to compare the electrical properties of the oxygen-deficient $SrTiO_{3-\delta}$ layer with those of the widely used transparent conducting layer, indium tin oxide (ITO). For ITO samples with a thickness of 50-100 nm, the resistivity is several hundred $\mu\Omega$ cm, while the mobility is 20 $cm^2\ V^{-1}\ s^{-1}$ and the carrier density is 10^{21} cm^{-3} [9, 10]. Therefore, the oxygen-deficient $SrTiO_{3-\delta}$ layer is equivalent to ITO.

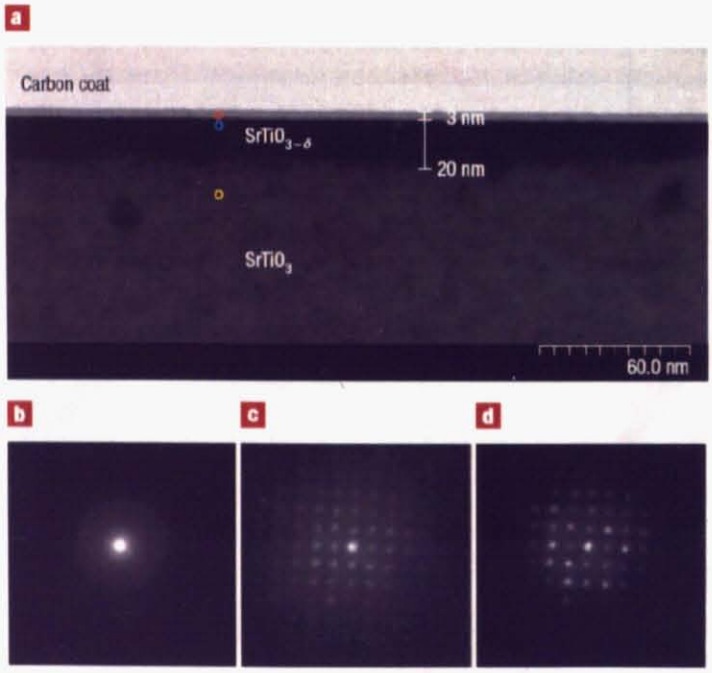

Figure4.9 (a) Cross-sectional TEM image taken after Ar ion milling for 5 min at an acceleration voltage of 300 V at 3 ml/min gas flow rate. (b)-(d) ED images taken from the topmost surface region of the amorphous layer with ~ 3nm thickness (red circle) (b), the oxygen-deficient layer below the amorphous layer (blue circle) (c), and the region far below the milled surface (yellow circle) (d) [Ref. 6].

4-2 Conclusions

For developing a new transistor fabrication process, I used thin layers of conducting $SrTiO_3$ that were fabricated by selective Ar ion milling to define the source and drain electrodes.

Oxygen-deficient $SrTiO_{3-\delta}$ was formed by Ar ion milling at an acceleration voltage of 500 V. It could be confirmed that the presence of step-and-terrace surface was destroyed by the accelerated Ar ions and that milling is an efficient way of introducing oxygen vacancies into a thin surface layer of $SrTiO_3$. These vacancies function as donors, inducing metallic conductivity in the electrode regions. The conducting layers might be very thin and cannot be detected with an optical spectrometer.

The oxygen-deficient $SrTiO_{3-\delta}$ layers had good thermal stability. The sheet carrier densities of all samples were close to 10^{14}. The mobilities were higher than 2 $cm^2 V^{-1} s^{-1}$ at room temperature and increased to 1000 $cm^2 V^{-1} s^{-1}$ at low temperature. These electrical properties are adequate for the use of oxygen-deficient $SrTiO_{3-\delta}$ layers as source and drain electrodes in $SrTiO_3$ field effect transistors.

References

1. O.N.Tufte and P.W.Chapman, Phys. Rev. **155**, 796 (1967).
2. C. M. Cooper, P. S. Nayar, E. B. Hale and R. Gerson, J. Appl. Phys. **50**, 2826 (1979).
3. J. Albrecht, S. Leonhardt, R. Spolenak, U. Täffner, H. -U. Habermeier and G. Schütz, Surf. Sci. **547**, L847 (2003).
4. B. Yang, P. D. Townsend, and R. Fromknecht, Nucl. Instrum. Methods. Phys. Res. **B226**, 549 (2004).
5. W. Reagor and V. Butko: Nat. Mater. **8**, 593 (2005).
6. D. Kan, T. Terashima, R. Kanda, A. Masuno, K. Tanaka, S. Chu, H. Kan, A. Ishizumi, Y. Kanemitu, Y. Shimakawa and M. Takano: Nat. Mat.**11**, 816 (2005).
7. K.Shibuya, T.Ohnishi, M.Lippmaa, M.Kawasaki and H.Koinuma, Appl. Phys. Lett. **85**, 425 (2004).
8. K.Shibuya, T.Ohnishi, T.Uozumi, T.Sato, M.Lippmaa, M.Kawasaki and H.Koinuma, Appl. Phys. Lett. **88**, 212116 (2006).
9. D. Wenli, T. Ohgi, H. Nejo and D. Fujita: Jpn. J. Appl. Phys. **40**, 3364 (2001).
10. T. Maruyama and K. Fukui: J. Appl. Phys. **70**, 3848 (1991).

Chapter 5

Fabrication and insulating properties of amorphous and epitaxial $CaHfO_3$ films

5-1 Introduction

Amorphous and epitaxial $CaHfO_3$ layers have been used as gate insulators in $SrTiO_3$ based FETs [1] because $CaHfO_3$ is a wide-gap insulator, it has a high dielectric constant, and a small lattice mismatch with $SrTiO_3$. Due to these reasons, the material offers low lea currents, large induced charge in a transistor gate stack, and is compatible with a fully epitaxial device structure. The lattice constant and mismatch data of $SrTiO_3$ and $CaHfO_3$ are listed in Table 5.1 [2,3]. The average mismatch with $SrTiO_3$ is about 2.3%. The band gap of $CaHfO_3$ is not well known, especially in thin films. Estimates based on the values published [4] for HfO_2, put the gap width above 5eV. Band-gap engineering is also possible when an insulator with a gap width above 5eV is combined with $SrTiO_3$. The conduction band offset with $SrTiO_3$ is expected to be 1.5eV, as shown in Figure 5.1. The wide band gap and band offset are useful for a gate insulator material because it is possible to achieve lower leak currents.

	Lattice constant (Å)					
SrTiO3 (cubic)	3.905	3.905	3.905			
	a	b	c	psudo-cubic $\sqrt{a^2+b^2}/2$, $c/2$		
CaHfO3 [3] (orthorhombic)	5.578	5.719	7.982	3.994	3.991	average mismatch
				2.28%	2.20%	2.30%

Table 5.1 Lattice constant of $SrTiO_3$ and $CaHfO_3$ [3]. The pseudo-cubic lattice constant and mismatch between $CaHfO_3$ and $SrTiO_3$ is also shown.

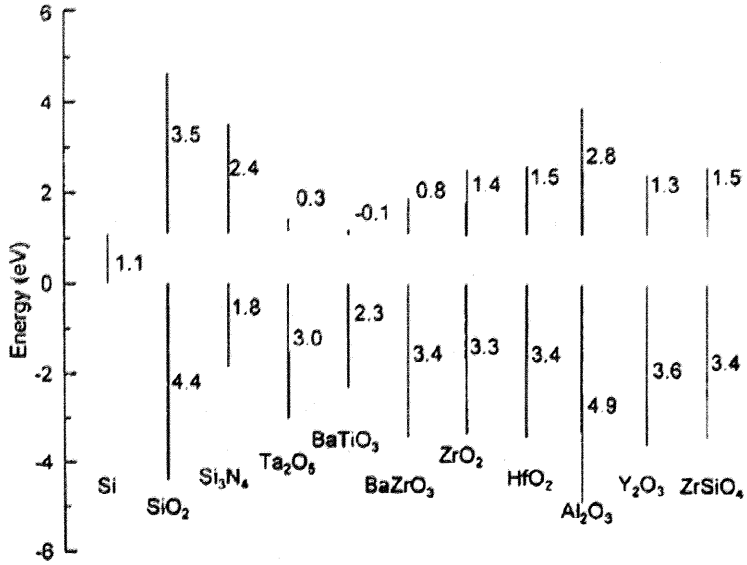

Figure 5.1 Calculated conduction band offsets of various oxides on Si [Ref.4].

5-2 Fabrication and insulating properties of $CaHfO_3$ films

I fabricated gate insulator films by pulsed laser deposition (PLD). PLD is a versatile thin film deposition technique and the main advantage of PLD is the nearly stoichiometric transfer of material from a solid target with the desired stoichiometry to the growing film. The PLD process conditions need to be carefully optimized, because changes in the growth rate, substrate temperature, and other parameters can have a strong effect on the properties of fabricated thin films. Due to this, the electrical breakdown strength of amorphous $CaHfO_3$ films was studied in films prepared under different PLD conditions.

A series amorphous $CaHfO_3$ films were fabricated to find the best PLD conditions for fabricating the gate insulator layer. The amorphous $CaHfO_3$ films were grown on Nb-doped $SrTiO_3$ (100) substrates (0.5 w.t.%). Here I show the carrier density in terms of the Nb-doped $SrTiO_3$ (100) substrate. Figure 5.2 shows measured carrier concentration of 0.5 and 0.05 w.t.% Nb-doped $SrTiO_3$ substrate at several temperatures. There is no carrier freezeout at low temperatures and the carrier densities are high enough for use as a bottom electrode in the breakdown field tests.

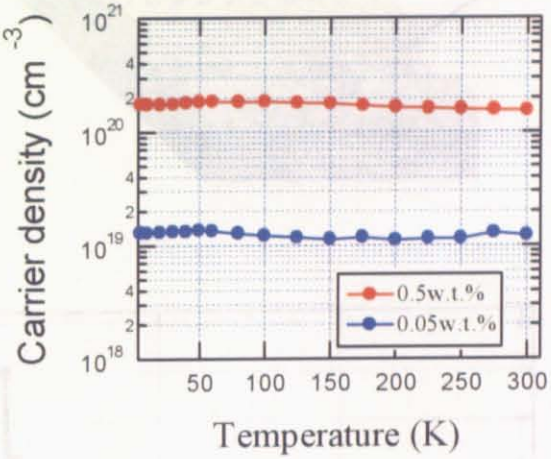

Figure 5.2 Temperature dependence of carrier density of (0.5 and 0.05 w.t. %) Nb-doped $SrTiO_3$ substrates.

The breakdown fields of amorphous $CaHfO_3$ films were measured by fabricating capacitor structures. The capacitor structure to measure the breakdown fields is shown in Figure 5.3 (a). Aluminum pads with a surface area of 0.03 mm^2 were evaporated on the films through a stencil mask and a capacitor structure was formed for current-voltage measurements. A typical leak current density of a 60 nm thick amorphous $CaHfO_3$ film is plotted as a function of the bias field in figure 5.3 (b). A breakdown was seen at 2.8 MV/cm. the breakdown field was measured at about 100 points on the sample surface. Histograms showing the breakdown field distributions of the films are plotted in Figure 5.4 (a), (b), and (c). The average breakdown field was determined by fitting the histograms with Gaussian curves. In Figure 5.4 (a), there are two Gaussian-type distributions of high and low electrical strength. These experiments showed that the best growth rate for amorphous $CaHfO_3$ films is 0.067 Å/pulse.

(a)

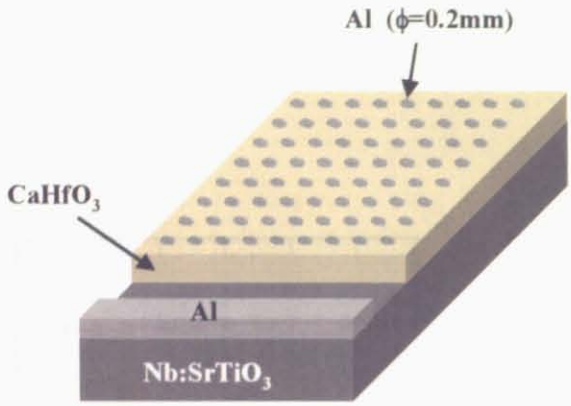

(b)

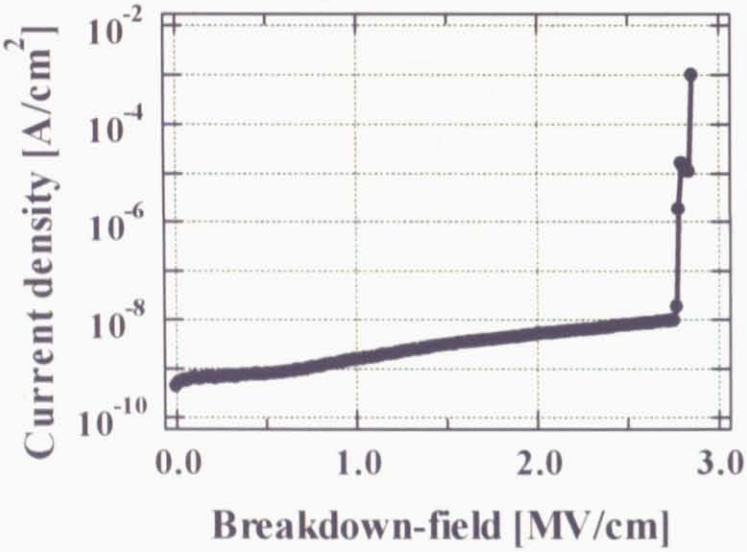

Figure 5.3 (a) Schematic drawing of a capacitor structure for electrical measurements. (b) A typical current-voltage curve of an amorphous $CaHfO_3$ film grown at an oxygen pressure of 3 mTorr.

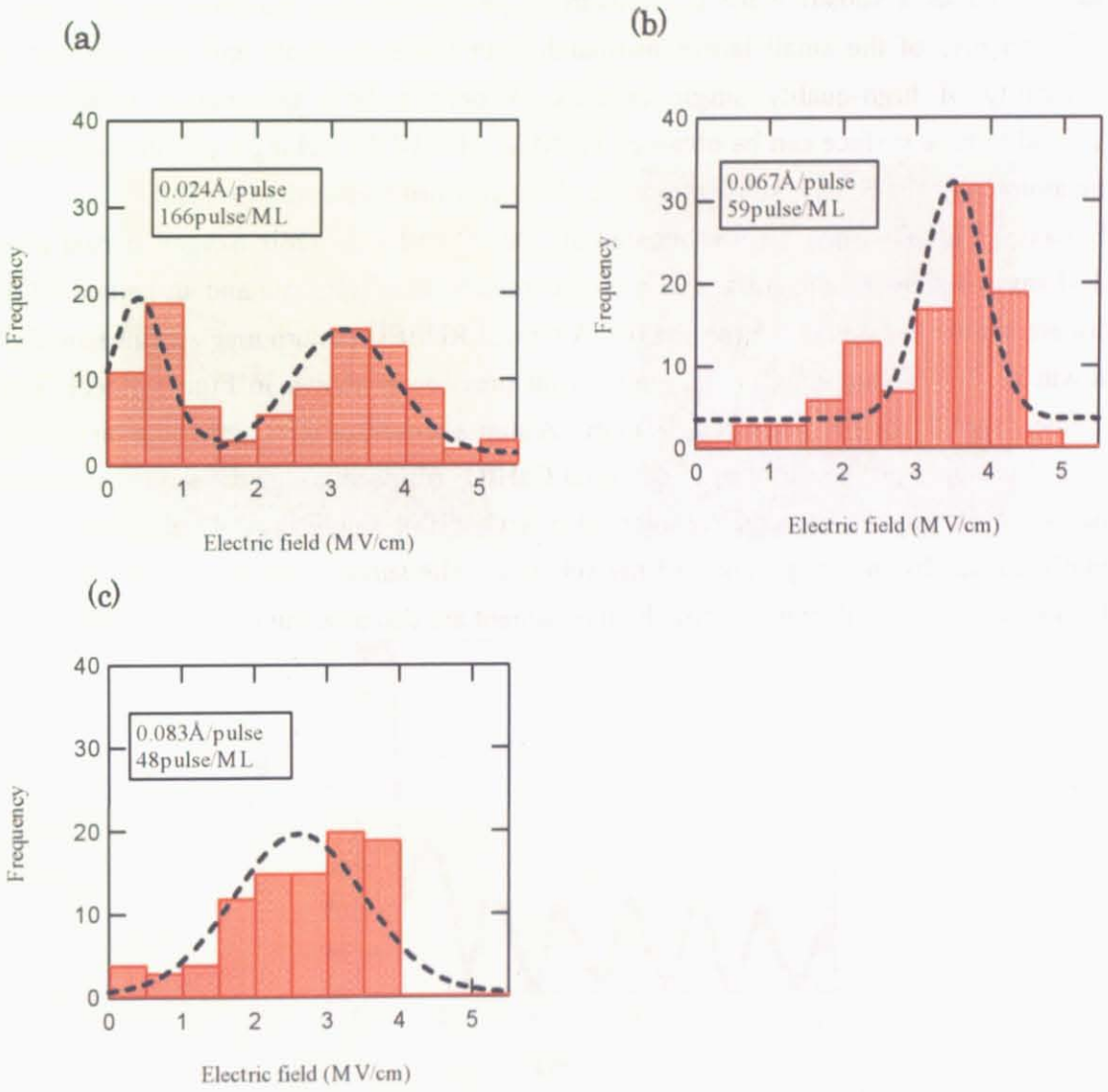

Figure 5.4 Histograms of breakdown fields of amorphous $CaHfO_3$ films fabricated at (a) 0.024, (b) 0.067, (c) 0.083 Å/pulse.

5-3 Growth of epitaxial $CaHfO_3$ films

Epitaxial $CaHfO_3$ films were grown on $SrTiO_3$ (100) single crystal substrates. $SrTiO_3$ is widely used as a substrate for the growth of perovskite-type transition-metal oxide films partly because of the small lattice mismatch with these materials and also because of the availability of high-quality single crystals. A perfect TiO_2 termination with molecular step-and-terrace surface can be obtained by NH_4F-HF (BHF) etching a polished substrate [5]. The atomically flat $SrTiO_3$ substrates were obtained from Shinkosha Co., Ltd.

Epitaxial $CaHfO_3$ films were fabricated at 700 °C and a 1 mTorr oxygen partial pressure. AFM images showing the surface of a commercial $SrTiO_3$ substrate and an epitaxial $CaHfO_3$ film are shown in Figures 5.5 (a) and (b). A typical RHEED pattern that was measured during growth at 700 °C and 1 mTorr oxygen partial pressure is shown in Figure 5.5(c). The KrF excimer laser fluence was about 0.68 J/cm^2. A step-and-terrace structure could be observed in the AFM images on the surfaces of epitaxial $CaHfO_3$ films, although the terrace structure was not as regular as that seen on commercial $SrTiO_3$ (100) single crystal substrates. This was mainly caused by the temperature of the substrate. The surface changes that occur in $SrTiO_3$ (100) single crystal substrates during heat treatment are discussed in the next section.

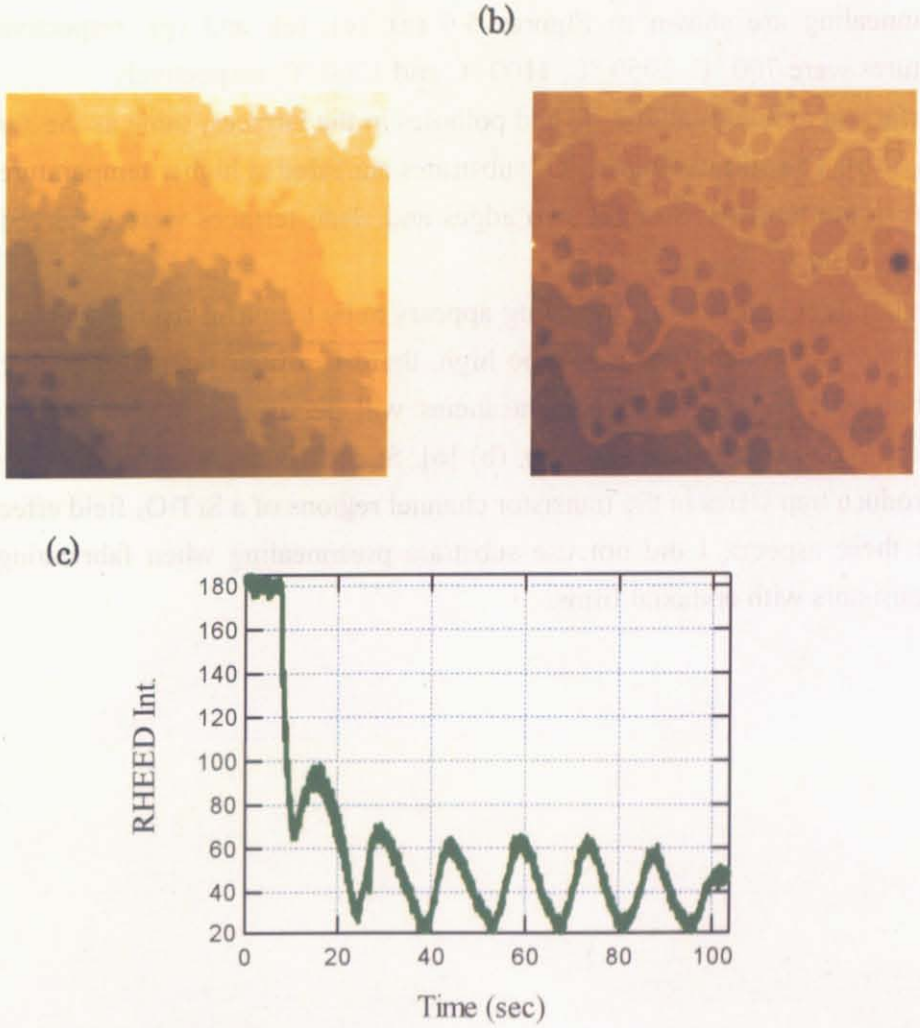

Figure 5.5 AFM images of surface of a commercial $SrTiO_3$ substrate (a) and epitaxial $CaHfO_3$ film (b). The image sizes are 1×1 μm^2. (c) Typical RHEED intensity oscillation observed during the growth of epitaxial $CaHfO_3$ films on $SrTiO_3$ (100) single crystal substrates.

5-2 $SrTiO_3$ substrates

Typical surface morphologies of $SrTiO_3$ (100) single crystal substrates obtained after annealing in the PLD chamber at 1 mTorr partial oxygen pressure for 1 hour are shown in Figures 5.6 (b), (d), (f), and (h). The surface morphologies of $SrTiO_3$ single crystal substrates before annealing are shown in Figures 5.6 (a), (c), (e), and (g), respectively. Annealing temperatures were 700 °C, 1050 °C, 1100 °C and 1200 °C, respectively.

The surface of a $SrTiO_3$ at 700 °C had potholes in the terraces, same as the surface shown in Figure 5.5 (b). The surfaces of $SrTiO_3$ substrates annealed at higher temperatures did not have the holes in the terraces. Straight step edges and clean terraces were observed on substrates annealed at 1100 °C and 1200°C.

Although higher temperature annealing appears to be beautiful from the point of view of the step structure, if the temperature is too high, there is a high degree of probability that SrO segregation will occur and oxygen vacancies will be formed in the $SrTiO_3$ single crystal substrates, as shown in Figure 5.7 (a), (b) [6]. Such SrO segregation and oxygen vacancies might produce trap states in the transistor channel regions of a $SrTiO_3$ field effect transistors.

Due to these aspects, I did not use substrate preannealing when fabricating $SrTiO_3$ field effect transistors with epitaxial films.

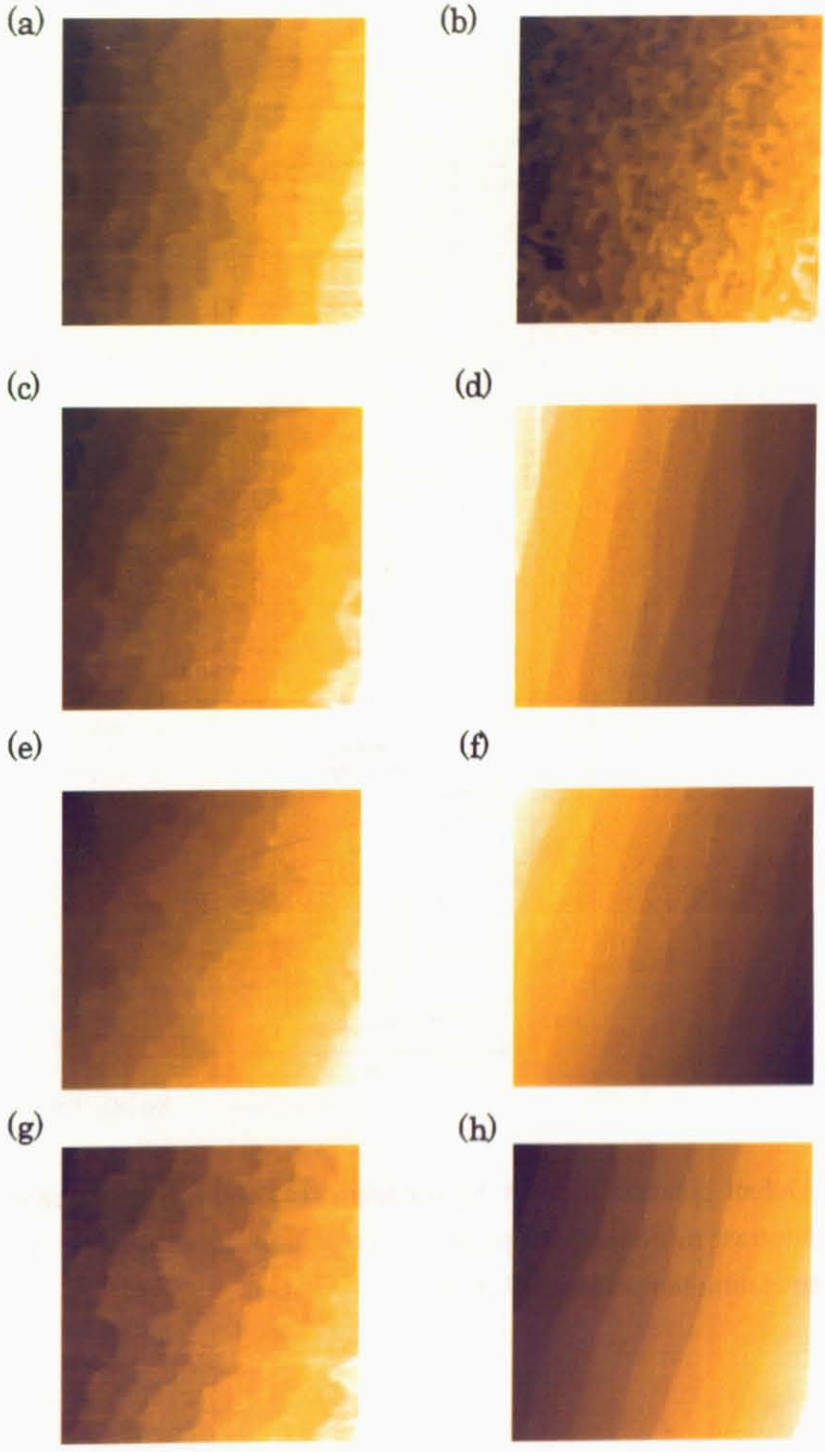

Figure 5.6 The surface morphologies of $SrTiO_3$ single crystal substrates before annealing (a), (c), (e), (g) and after annealing for 1 hour at 700 °C (b), 1050 °C (d), 1100 °C (f) and 1200 °C (h). The image sizes are 1×1 μm^2.

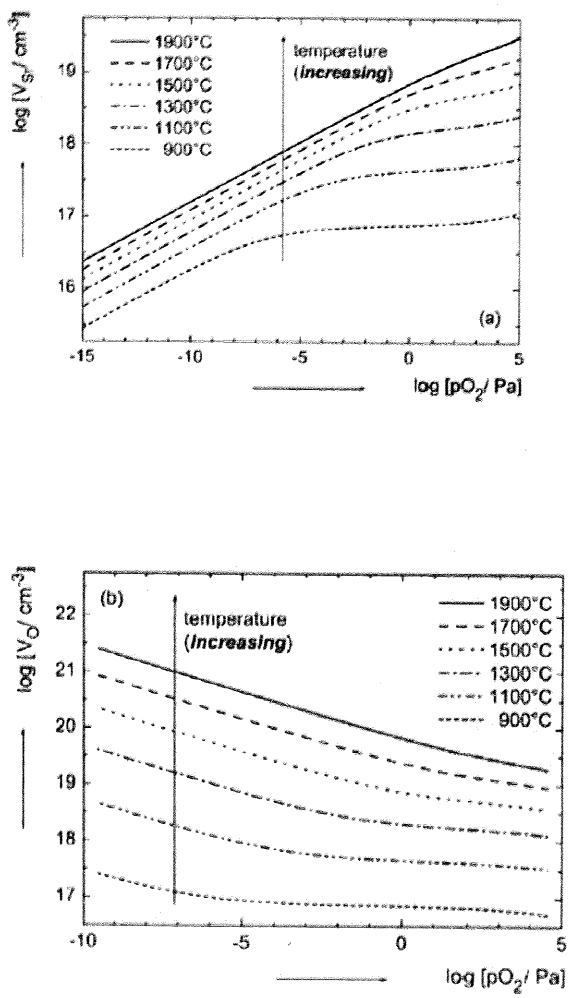

Figure 5.7 Defect concentration of Sr vacancies (a) and oxygen vacancies (b) in undoped $SrTiO_3$. In contrast to donor-doping, the concentration of both defect species increases with increasing annealing temperature [Ref. 6].

5-3 Conclusion

Wide-gap insulator film, $CaHfO_3$, was fabricated on $SrTiO_3$ (100) single crystal substrates. The breakdown fields of amorphous $CaHfO_3$ films were measured by fabricating capacitor structures. The Histograms showing the breakdown field distributions of the films was plotted. The average breakdown field was determined by fitting the histograms with Gaussian curves. Therefore, these experiments showed that the best growth rate for amorphous $CaHfO_3$ films is 0.067 Å/pulse. The average breakdown was seen at 3.9 MV/cm.

Epitaxial $CaHfO_3$ films were grown on $SrTiO_3$ (100) single crystal substrates. Epitaxial $CaHfO_3$ films were fabricated at 700 °C and a 1 mTorr oxygen partial pressure. A step-and-terrace structure could be observed in the AFM images on the surfaces of epitaxial $CaHfO_3$ films, although the terrace structure was not as regular as that seen on commercial $SrTiO_3$ (100) single crystal substrates.

To understand these, I checked the surface morphologies of $SrTiO_3$ (100) single crystal substrates obtained after annealing in the PLD chamber at 1 mTorr partial oxygen pressure for 1 hour. Annealing temperatures were 700 °C, 1050 °C, 1100 °C and 1200 °C. Due to these results, I understood that the surface changes that occur in $SrTiO_3$ (100) single crystal substrates during heat treatment. But, if the temperature is too high, there is a high degree of probability that SrO segregation will occur and oxygen vacancies will be formed in the $SrTiO_3$ single crystal substrates.

Due to these aspects, I could decide not to use substrate preannealing when fabricating $SrTiO_3$ field effect transistors with epitaxial films.

References

1. K.Shibuya, T.Ohnishi, T.Uozumi, T.Sato, M.Lippmaa, M.Kawasaki and H.Koinuma, Appl. Phys. Lett. **88**, 212116 (2006).
2. K.H.Hellwege, A.M.Hellwege Science and Technology New Series, Group III, **Vol.16a**, 59-64 (Springer, Berlin, 1981).
3. K.Shibuya, T.Ohnishi, M.Lippmaa, M.Kawasaki and H.Koinuma, Appl. Phys. Lett. **85**, 425 (2004).
4. J. Robertson, J. Vac. Sci. Technol. **B 18**, 1785 (2000).
5. M.Kawasaki, K.Takahashi, T.Maeda, R.Tsuchiya, M.Shinohara, O.Ishiyama, T.Yonezawa, M.Yoshimoto and H.Koinuma, Science **266**, 1540 (1994).
6. R.Meyer, R. Waser, J. Helmbold and G Borchardt, J.Electroceramics .**9**.101 (2002).